Hydrogen Evolution Reaction | Very Important Paper

How to cite: Angew. Chem. Int. Ed. 2023, 62, e202212653
International Edition: doi.org/10.1002/anie.202212653
German Edition: doi.org/10.1002/ange.202212653

Tuning Mass Transport in Electrocatalysis Down to Sub-5 nm through Nanoscale Grade Separation

Zhenhui Liu[+], Yue Du[+], Ruohan Yu[+], Mingbo Zheng, Rui Hu, Jingsong Wu, Yongyao Xia, Zechao Zhuang, and Dingsheng Wang**

Abstract: Nano and single-atom catalysis open new possibilities of producing green hydrogen (H_2) by water electrolysis. However, for the hydrogen evolution reaction (HER) which occurs at a characteristic reaction rate proportional to the potential, the fast generation of H_2 nanobubbles at atomic-scale interfaces often leads to the blockage of active sites. Herein, a nanoscale grade-separation strategy is proposed to tackle mass-transport problem by utilizing ordered three-dimensional (3*d*) interconnected sub-5 nm pores. The results reveal that 3*d* criss-crossing mesopores with grade separation allow efficient diffusion of H_2 bubbles along the interconnected channels. After the support of ultrafine ruthenium (Ru), the 3*d* mesopores are on a superior level to two-dimensional system at maximizing the catalyst performance and the obtained Ru catalyst outperforms most of the other HER catalysts. This work provides a potential route to fine-tuning few-nanometer mass transport during water electrolysis.

Introduction

Electrochemical water splitting powered by renewables opens numerous possibilities for scalable production of green hydrogen.[1] To improve electrolyzer efficiency, the cathodic hydrogen evolution reaction (HER) requires an electrocatalyst that allows not only the efficient reduction of protons to H_2 but also the facile detachment of H_2 bubbles from the surface to avoid their blockage of the active sites.[2,3] These two requirements become crucial, when water electrolysis cells operate at $A\,cm^{-2}$.[4] Therefore, the rational design of HER catalysts brings practical meaning to producing hydrogen from water.[5]

Over a decade of effort by scientists have been expended on this goal, with much of that focused on increasing the number of active sites of catalysts or improving the intrinsic activity.[6] Across multiple length scales, optimization strategies are being proposed, for example defect or phase engineering,[7,8] nanostructuring,[9] and design of heterostructure.[10] However, controlling mass transport at the solid–liquid–gas interface of H_2 evolution is more challenging, and does not advance as far.[11] Compared with gas-concentration-limited cathodic reactions (for example, the reduction of O_2 and CO_2), the HER possesses a much greater reaction rate by several orders of magnitude.[12] For an active catalyst, the fast generation of H_2 may form plenty of gas bubbles attached on the catalyst surface, which block the active sites[13] and enlarge the ohmic resistance of the electrolyte,[14] leading to voltage loss in electrolyzer. Recently, some electrode structures featuring a superaerophobic surface and good electrolyte wettability were well designed—catalyst-coated membranes,[15] fibrous catalyst layers,[16] nanoarrays,[17] and macroporous frameworks[18]—to minimize bubble growth and accelerate detachment, although they usually failed to regulating mass transport at the nanometer scale (Figure 1).[19] When metal catalysts are downsized to a few nanometers, even to the single-atom limit,[20] the above-mentioned structures cannot provide matching transport channels for the ultrasmall nanobubbles generated by electrolysis at atomic-scale interfaces.[21] The low transport efficiency, in turn, limits the practicalities of nano-and single-atom catalysts for HER.[22] Consequently, developing a new strategy to achieve few-nanometer confined mass transport is urgently required.[23]

Herein, we propose a nanoscale grade-separation strategy to achieve confined mass transport at the few-nanometer through utilization of ordered three-dimensional (3*d*) interconnected sub-5 nm pores (rightmost panel of Figure 1). Specifically, two types of catalyst carbon supports were synthesized that showed either two-dimensional (2*d*) hexagonal ($p6m$) or 3*d* cubic ($Im\bar{3}m$) ordered mesopores of

[*] Dr. Z. Liu,[+] Prof. M. Zheng, R. Hu, Prof. Y. Xia
College of Material Science and Engineering,
Nanjing University of Aeronautics and Astronautics
Nanjing, 210016 (P. R. China)

Dr. Z. Zhuang, Prof. D. Wang
Department of Chemistry, Tsinghua University
Beijing (P. R. China)
E-mail: zhuangzc@mail.tsinghua.edu.cn
wangdingsheng@mail.tsinghua.edu.cn

Dr. Y. Du[+]
Institute for Advanced Materials,
Hubei Normal University
Huangshi, 435002 (P. R. China)

R. Yu,[+] Prof. J. Wu
Wuhan University of Technology,
Nanostructure Research Centre
Wuhan, 430070 (P. R. China)

Prof. Y. Xia
Department of Chemistry, Fudan University
Shanghai, 200433 (P. R. China)

[+] These authors contributed equally to this work.

© 2022 Wiley-VCH GmbH

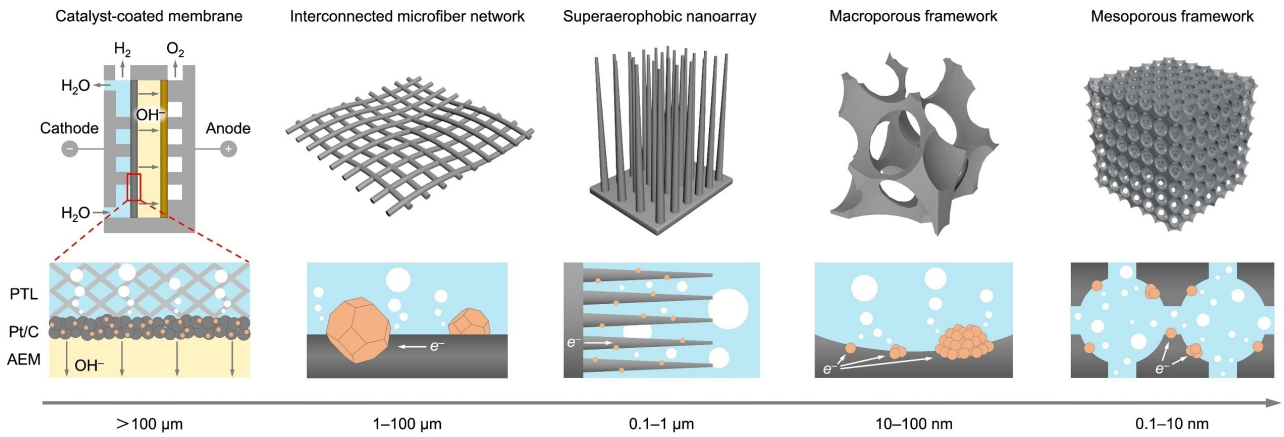

Figure 1. Schematic diagrams of H_2 gas diffusion on catalyst–electrolyte interface for different types of electrode structures.

about 4–5 nm width (named 2*d*-OMC and 3*d*-OMC). The pores below 5 nm perfectly match the size of nanobubbles that evolve on few-nanometer catalysts. In 2*d*-OMC, the mesopore channels are parallel to each other over long distances, through which gas bubbles can only diffuse out in the axial direction. But, 3*d*-OMC is a lattice of criss-crossing pores with grade separation in three dimensions, which is similar to grade-separated junctions in urban and rural areas, thus allowing bubbles to move freely along these interconnected channels, with fewer interruptions, and at higher overall transport rates. After ultrafine ruthenium (Ru) being supported on, the 3*d* arrangement of pores was, indeed, on a superior level to 2*d* system in transport efficiency for H_2; Ru/3*d*-OMC exhibits an over twofold improvement in catalytic activity than that of Ru/2*d*-OMC, even outperforming most other state-of-the-art HER catalysts. Our comparative study deepens our understanding on few-nanometer mass transport during water electrolysis, and offers a promising strategy how to control it.

Results and Discussion

Our strategy for preparing Ru/3*d*-OMC involves surfactant-templated self-assembly, in which F127 (poly(ethylene oxide)-poly(propylene oxide)-poly(ethyleneoxide) triblock copolymer) acts as a structure-directing agent for the condensation of organic species. In this system, hexamethylenetetramine (HMT) can decompose into formaldehyde and ammonia, and 3-aminophenol possesses strong hydrogen-bond interaction with F127. Therefore, F127 can be combined with formaldehyde and 3-aminophenol using an organic sol–gel process to form a self-ordered 3-aminophenol-formaldehyde/F127 product (APF/F127) (Figure S1). Next, the as-synthesized APF/F127 was redispersed in an aqueous solution of $RuCl_3$ at room temperature, and the Ru^{3+} ions can be trapped by rich nitrogen (N)-containing organo-functional groups in APF. Subsequent carbonization and removal of F127 templates yielded Ru/3*d*-OMC with ordered 3*d* interconnected mesopores and uniform dispersion of ultrafine Ru particles. Mesoporous structures fabricated using such a soft-template possess stable cylindrical mesopore channels, which are beneficial for the smooth mass transfer of H_2. Ru/2*d*-OMC was synthesized under similar conditions, except an amount of 1,3,5-triethylbenzene (TMB) was added in the cooperative self-assembly process. TMB tends to distribute in the hydrophobic regions of polymeric micelles, leading to the decrease of the hydrophilic/hydrophobic volume ratio and the interfacial curvature. When the balance of hydrophilic/hydrophobic is achieved, a transformation of mesoporous structure from $Im\bar{3}m$ to $p6m$ occurs (Figure S2). According to the scanning electron microscope (SEM) images, one could observe that the Ru/2*d*-OMC possessed rod-like morphologies (Figure S3) whereas Ru/3*d*-OMC exhibited irregular shapes with particle sizes range from hundreds of nanometers to micrometers (Figure S4).

To further investigate mesopore structures, Ru/2*d*-OMC and Ru/3*d*-OMC were characterized through small-angle X-ray scattering (SAXS) patterns.[24] As shown in Figure 2a, the SAXS pattern of Ru/2*d*-OMC showed three peaks, which could be attributed to (10), (11), and (20) reflections, revealing the typical 2*d* hexagonal symmetry of Ru/2*d*-OMC. The position of the strong (10) peak indicated a *d*-spacing of 10.2 nm, corresponding to a unit cell parameter of 11.8 nm, which was calculated according to the Formulas (1) and (2):

$$d_{(10)} = 2\pi/q \tag{1}$$

$$a_0 = 2d_{(10)}/\sqrt{3} \tag{2}$$

The SAXS pattern of Ru/3*d*-OMC exhibited one intense peak of (110) and two weak peaks of (200) and (211), which was coincident with the typical features of body-centered cubic structure. The lattice *d*-spacing of Ru/3*d*-OMC and corresponding unit cell parameter was calculated to be 8.7 nm and 12.3 nm, respectively, according to the Formulas (3) and (4):

$$d_{(110)} = 2\pi/q \tag{3}$$

© 2022 Wiley-VCH GmbH

15213773, 2023, 3, Downloaded from https://onlinelibrary.wiley.com/doi/10.1002/anie.202212653 by University Of Adelaide, Wiley Online Library on [29/06/2024]. See the Terms and Conditions (https://onlinelibrary.wiley.com/terms-and-conditions) on Wiley Online Library for rules of use; OA articles are governed by the applicable Creative Commons License

$$a_0 = (\sqrt{2})d_{(110)} \quad (4)$$

TEM images of Ru/2*d*-OMC (Figures 2b and c) viewed along the [001] and [110] directions confirmed the 2*d* hexagonal ordered mesoporous structure with parallel long-range pore channels. The cell parameter measured from the TEM image was 12.2 nm. The N_2 adsorption isotherm and pore size distribution curve suggested that cylindrical ordered mesopores with size of 4.7 nm were generated in Ru/2*d*-OMC by adopting F127 as soft template. Compared with random mesopores, ordered mesopores possess uniform pore sizes, relatively straight, and open pore channels, which are more beneficial to the mass transport of H_2. The corresponding specific BET surface area and pore volume of Ru/2*d*-OMC were 325 $m^2 g^{-1}$ and 0.28 $m^3 g^{-1}$, respectively (Figures S5a and S5b). TEM images viewed from [111], [100], and [110] directions (Figures 2d–f) revealed that Ru/3*d*-OMC possessed highly ordered periodic mesopores with interconnected channels. The cell parameter estimated from TEM images was approximately 12.5 nm. The BET surface area and the total pore volume of Ru/3*d*-OMC were calculated to be 368 $m^2 g^{-1}$ and 0.28 $cm^3 g^{-1}$, respectively. The pore distribution curve showed that there was a narrow strong peak located in 5.1 nm (Figures S5c and S5d). Such pore size is suitable for the rapid release of ultrafine nanobubbles generated at atomic-scale interfaces. Compared with mesopores, larger confined space of macropores may lead the ultrasmall nanobubbles to accumulate into larger bubbles that are difficult to be diffused out and may block the catalytically active sites.

To better understand the structures of Ru/2*d*-OMC and Ru/3*d*-OMC, powerful atomic electron tomography was applied.[25] As shown in Figure 2g, the electron beam was

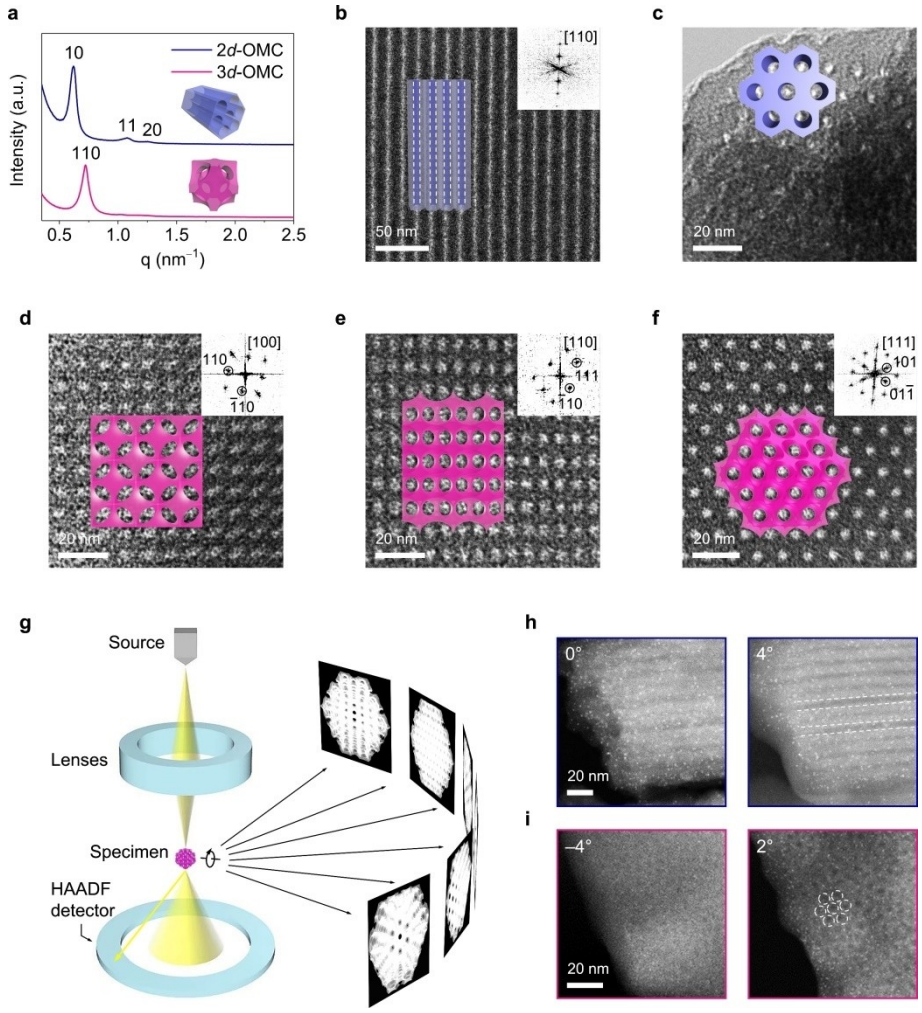

Figure 2. a) SAXS patterns of Ru/2*d*-OMC and Ru/3*d*-OMC. Insets show the corresponding mesoporous structures; b), c) TEM images of Ru/2*d*-OMC viewed in the [110] (b) and [001] directions (c). d)–f) TEM images of Ru/3*d*-OMC viewed in the [100] (d), [110] (e), and [111] directions (f). Insets of (b)–(f) show the corresponding mesoporous structures and fast Fourier transform (FFT) diffractograms in different planes; g) Schematic diagram of electron microscope tomography, in which 2*d* images are measured with an advanced electron microscope by tilting a sample to many different orientations. TEM images viewed in different directions can be obtained; h), i) TEM images of Ru/2*d*-OMC (h) and Ru/3*d*-OMC particles (i) measured at different tilt angles. Dotted lines in (h) mark the parallel channels of Ru/2*d*-OMC, while dotted cycles in (i) mark the mesopores viewed in the [111] direction of Ru/3*d*-OMC.

© 2022 Wiley-VCH GmbH

15213773, 2023, 3, Downloaded from https://onlinelibrary.wiley.com/doi/10.1002/anie.202212653 by University Of Adelaide, Wiley Online Library on [29/06/2024]. See the Terms and Conditions (https://onlinelibrary.wiley.com/terms-and-conditions) on Wiley Online Library for rules of use; OA articles are governed by the applicable Creative Commons License

focused on a small spot and scanned over an individual particle sample to form a 2*d* image. By rotating the sample around a tilt axis, a series of 2*d* images could be obtained at different tilt angles, which could provide more comprehensive 3*d* structural information. From the Figure 2h and Movie S1, cylindrical ordered parallel mesopore channels of Ru/2*d*-OMC could be always observed, with the change in tilt angles, thus indicating that the pore channels in Ru/2*d*-OMC were non-interconnected, similar to the assembly of nanotubes. Both Figure 2i and Movie S2 showed rich and ordered distribution of mesopores on the Ru/3*d*-OMC individual particle. As the angle changed, mesopores in (111) and (110) planes could be observed respectively, further endorsing the 3*d* continuous interconnected mesopore channels in Ru/3*d*-OMC, which were expected to benefit the homogeneous dispersion of Ru species and accelerate the mass transport in HER.

X-ray diffraction (XRD) patterns of the Ru/2*d*-OMC and Ru/3*d*-OMC showed two broad peaks at approximately 23.7 and 44.2° (Figure S6), which were corresponding to the characteristics of carbon support, and no obvious characteristic peaks of Ru could be observed, indicating few-nanometer ultrafine Ru species disperse homogeneously on the ordered mesoporous carbon support. To further explore the existential form and coordination environment of Ru species, X-ray absorption fine structure (XAFS) measurements were conducted (Figures 3a, b, and S7). The Ru *K*-edge X-ray absorption near edge structure (XANES) spectra of Ru/3*d*-OMC and Ru/2*d*-OMC were presented in Figure 3a together with the spectra of Ru foil, $Ru(acac)_3$, and RuO_2. It was observed that the edges of Ru/3*d*-OMC and Ru/2*d*-OMC lay between those of Ru foil and RuO_2, elucidating that the average oxidation state of Ru/3*d*-OMC and Ru/2*d*-OMC was between 0 and +IV. From the extend XAFS (EXAFS) spectra in *R* space (Figure 3b), it could be observed that Ru–O bonds located at 1.54 and 1.50 Å in RuO_2 and $Ru(acac)_3$, respectively, while Ru–Ru bond located at 2.40 Å in Ru foil. Both Ru/2*d*-OMC and Ru/3*d*-

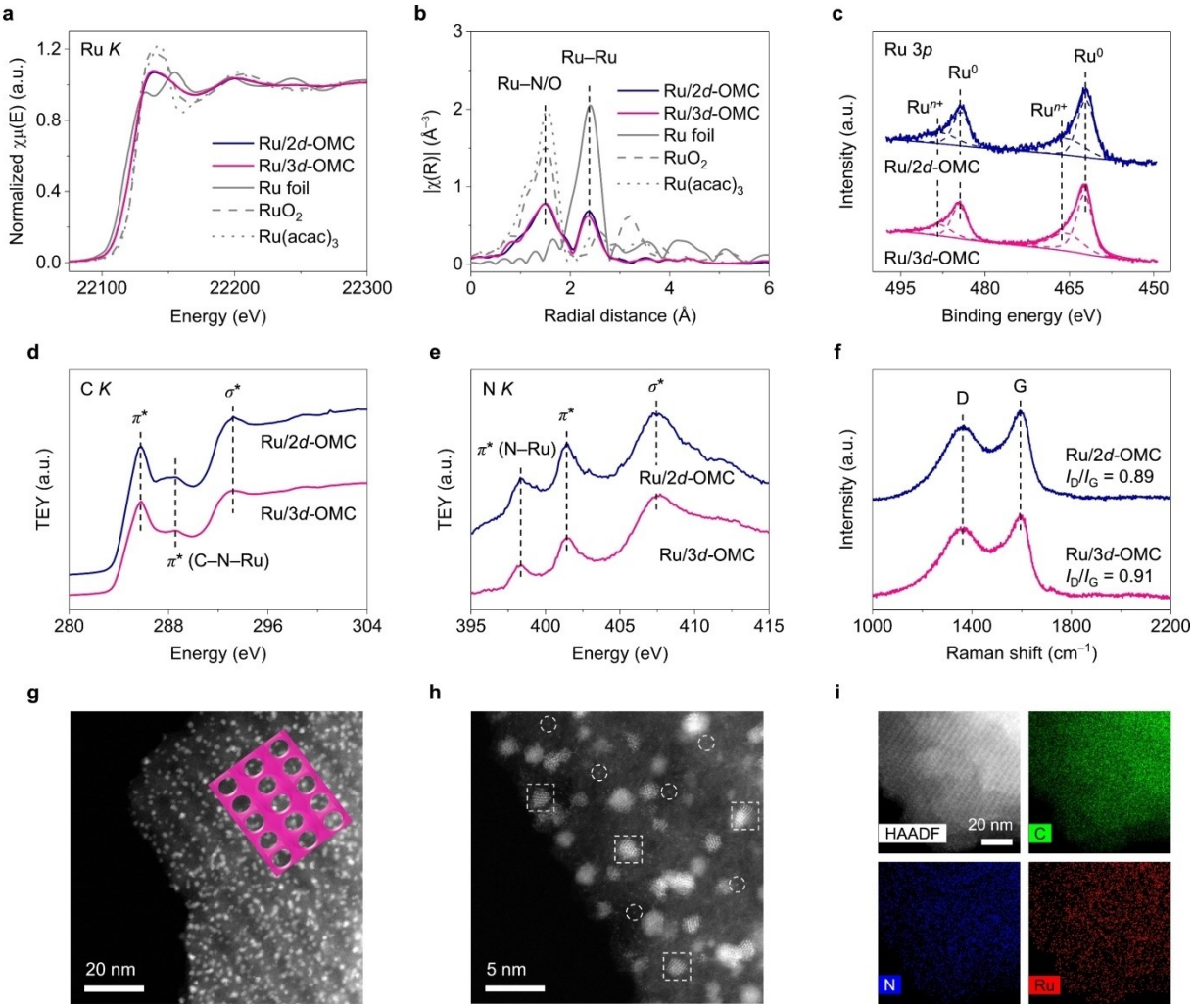

Figure 3. a) Normalized XANES spectra of Ru/2*d*-OMC, Ru/3*d*-OMC, Ru foil, RuO_2, and $Ru(acac)_3$; b) EXAFS spectra in *R* space; c) High-resolution Ru 3*p* XPS of Ru/2*d*-OMC and Ru/3*d*-OMC; d) C *K*-edge XANES spectra; e) N *K*-edge XANES spectra; f) Raman spectra; g), h) Dark-field HAADF-STEM image of Ru/3*d*-OMC. Inset of (g) shows the mesoporous structure of Ru/3*d*-OMC in [110] plane. Dotted boxes in (h) mark Ru nanoparticles, while dotted cycles mark single Ru atoms; i) EDS elemental mappings of Ru/3*d*-OMC.

© 2022 Wiley-VCH GmbH

15213773, 2023, 3, Downloaded from https://onlinelibrary.wiley.com/doi/10.1002/anie.202212653 by University Of Adelaide, Wiley Online Library on [29/06/2024]. See the Terms and Conditions (https://onlinelibrary.wiley.com/terms-and-conditions) on Wiley Online Library for rules of use; OA articles are governed by the applicable Creative Commons License

OMC exhibited similar EXAFS curves and displayed two major peaks at about 1.49 Å and 2.37 Å, which should be attributed to the Ru–N coordination and Ru–Ru bonding, respectively, indicating the coexistence of Ru single atoms and small Ru nanoparticles.[26] The X-ray photoelectron spectroscopy (XPS) survey spectra (Figures S8 and S9) confirmed that the existence of C, N, O, and Ru in Ru/2*d*-OMC and Ru/3*d*-OMC. Figure 3c showed the high-resolution Ru 3*p* spectra of the two samples, in which the peaks at 465.02 and 487.84 eV were attributed to the position of Ru^{n+} while other peaks corresponded to the form of Ru^0, among which the Ru^{n+} accounts for about 20.7 %.[27] According to previous reports,[18a] carbon supported Ru nanoparticles have been demonstrated to possess high intrinsic activity. Therefore, few-nanometer Ru nanoparticles are expected to plays a major catalytic role in this study. The high-resolution N 1*s* spectra (Figures S8a and S9a) could be deconvoluted into four parts, corresponding to pyridinic N (398.12 eV), pyrrolic N (400.02 eV), quaternary N (401.01 eV), and pyridine-N-oxide (403.21 eV). The C *K*-edge NEXAFS spectra of Ru/2*d*-OMC and Ru/3*d*-OMC (Figure 3d) displayed three distinct peaks at 285.6, 288.5, and 293.1 eV, respectively. These peaks were ascribed to the dipole transition of the C 1*s* core electron into the π^*(C=C), π^*(C–N), and σ^*(C–C) antibonding orbitals, respectively. The N chemical configurations of Ru/3*d*-OMC and Ru/2*d*-OMC were also investigated by the XANES of the N *K*-edge (Figure 3e). The peaks at 398.3, 399.4 and 401.4 eV could be attributed to pyridinic-, amino-, and pyrrolic-N, respectively, whereas the peak at 407.5 eV originated from graphitic-N. The immobilization of Ru species on the surface on N-doped carbon surfaces could lead the decrease in the π^* resonance intensity in N *K*-edge NEXAFS spectra. The weak peak at approximately 398.4 eV could be ascribed to the N species interacting with Ru.[28] Raman spectra (Figure 3f) of the Ru/2*d*-OMC and Ru/3*d*-OMC samples presented a broad peak at $\approx$1368 cm^{-1} and a relatively sharp peak at $\approx$1592 cm^{-1}, corresponding to the characteristic D band and G band of carbonaceous materials, respectively. Both the I_D/I_G ratios of the Ru/2*d*-OMC and Ru/3*d*-OMC were around 0.9, thus demonstrating the high degree of graphitization of the ordered mesoporous carbon support.[29]

In the high angle annular dark-field scanning transmission electron microscope (HAADF-STEM) of Ru/3*d*-OMC (Figure 3g), it could be observed that uniform few-nanometer Ru nanoparticles were uniformly anchored around the ordered mesopores (labelled by mesopore diagram of [110] plane). The atomic dispersion of Ru could be also directly monitored by HAADF-STEM. Ru atoms were confirmed by the monodispersed bright dots anchored at the surface of the 3*d*-OMC support, further confirming the coexistence of nanoparticles and single atoms. From HAADF-STEM images of Ru/2*d*-OMC (Figures S10a and S10b), it could be observed that few-nanometer Ru nanoparticles also distributed uniformly around the 2*d* parallel mesopore channels. Additionally, the co-coexistence of Ru nanoparticles and single atoms in Ru/2*d*-OMC was demonstrated by TEM images (Figures S10c and S10d), and it was similar to that of Ru/3*d*-OMC. Furthermore, from TEM images in Figures S11 and S12, the lattice fringe of graphitized carbon in Ru/2*d*-OMC and Ru/3*d*-OMC could be also clearly observed, indicating the high degree of graphitization of the carbon support, which was in accord with the Raman results. Both average particle sizes of Ru/2*d*-OMC and Ru/3*d*-OMC concentrated on $\approx$1.65 nm (Figure S13). The elemental mapping images (Figures 3i and S14) of Ru/3*d*-OMC further confirmed the homogeneous distribution of C, N, and Ru species.

Although numerous reports have demonstrated that porous structures endow catalysts with a large surface area and high mass transfer efficiency, the in-depth study of pore-structural effects on HER catalytic performance through comparative experiments remains limited. According to the characterization results, it can be indicated that Ru/2*d*-OMC and Ru/3*d*-OMC possess the similar BET surface areas, pore sizes, degrees of graphitization, and homogeneous distribution of Ru species, which can provide an idea platform on investigating the effects of pore structures on mass transfer in HER.

The electrocatalytic performances of the Ru/2*d*-OMC and Ru/3*d*-OMC catalysts were examined by a typical three-electrode electrochemical cell. Figure 4a showed linear sweep voltammetry (LSV) curves of Ru/2*d*-OMC, Ru/3*d*-OMC, and commercial Pt/C catalysts in 1 M KOH. As shown in Figure 4a, it could be observed that Ru/3*d*-OMC exhibited a small onset potential of nearly $\approx$0 mV versus the reversible hydrogen electrode (RHE) and achieved a current density of 10 mA cm^{-2} at a small overpotential of $\approx$20 mV, which was much lower than that of Pt/C (45 mV) and Ru/2*d*-OMC (65 mV) (Figure 4c). To further investigate the kinetics of HER, Tafel slopes were obtained via analyses of LSV curves (Figure 4b). Ru/3*d*-OMC showed a Tafel slope of 40.5 mV dec^{-1}, whereas Pt/C and Ru/2*d*-OMC exhibit Tafel slopes of 65.9 and 66.0 mV dec^{-1}, respectively. Such excellent catalytic activity of Ru/3*d*-OMC should be due to the structural advantages on rapid diffusion of H_2. When the current density increased to 50 mA cm^{-2}, the overpotentials of Ru/3*d*-OMC, Ru/2*d*-OMC and Pt/C were 104 mV, 215 mV, and 177 mV respectively. We have further investigated the electrochemically active surface areas (ECSAs) of Ru/3*d*-OMC and Ru/2*d*-OMC. The ECSA could be estimated from the cyclic voltammetry measurements, which was proportional to the double-layer capacitance (C_{dl}) of the catalyst. The result showed that both Ru/2*d*-OMC and Ru/3*d*-OMC possessed large and similar values of C_{dl} (Figure S15). The long-term durability of Ru/3*d*-OMC, Ru/2*d*-OMC, and commercial Pt/C was investigated by the chronoamperometric test under initial current density of 10 mA cm^{-2} (Figures S16–S18). After continuous running for 50 000 s, the current densities of Ru/3*d*-OMC and Ru/2*d*-OMC were maintained above 85 %, whereas that of Pt/C was maintained less than 60 %, which fully verified the excellent stability of OMC-supported Ru-based electrocatalysts. To unveil applicability of the resulting Ru catalysts under acidic condition, their performances were tested in 0.5 M H_2SO_4. As shown in Figure S19, Ru/3*d*-OMC exhibited excellent performance for HER in the acidic electrolyte as well, with a low overpotential of 38 mV at the current

© 2022 Wiley-VCH GmbH

15213773, 2023, 3, Downloaded from https://onlinelibrary.wiley.com/doi/10.1002/anie.202212653 by University Of Adelaide, Wiley Online Library on [29/06/2024]. See the Terms and Conditions (https://onlinelibrary.wiley.com/terms-and-conditions) on Wiley Online Library for rules of use; OA articles are governed by the applicable Creative Commons License

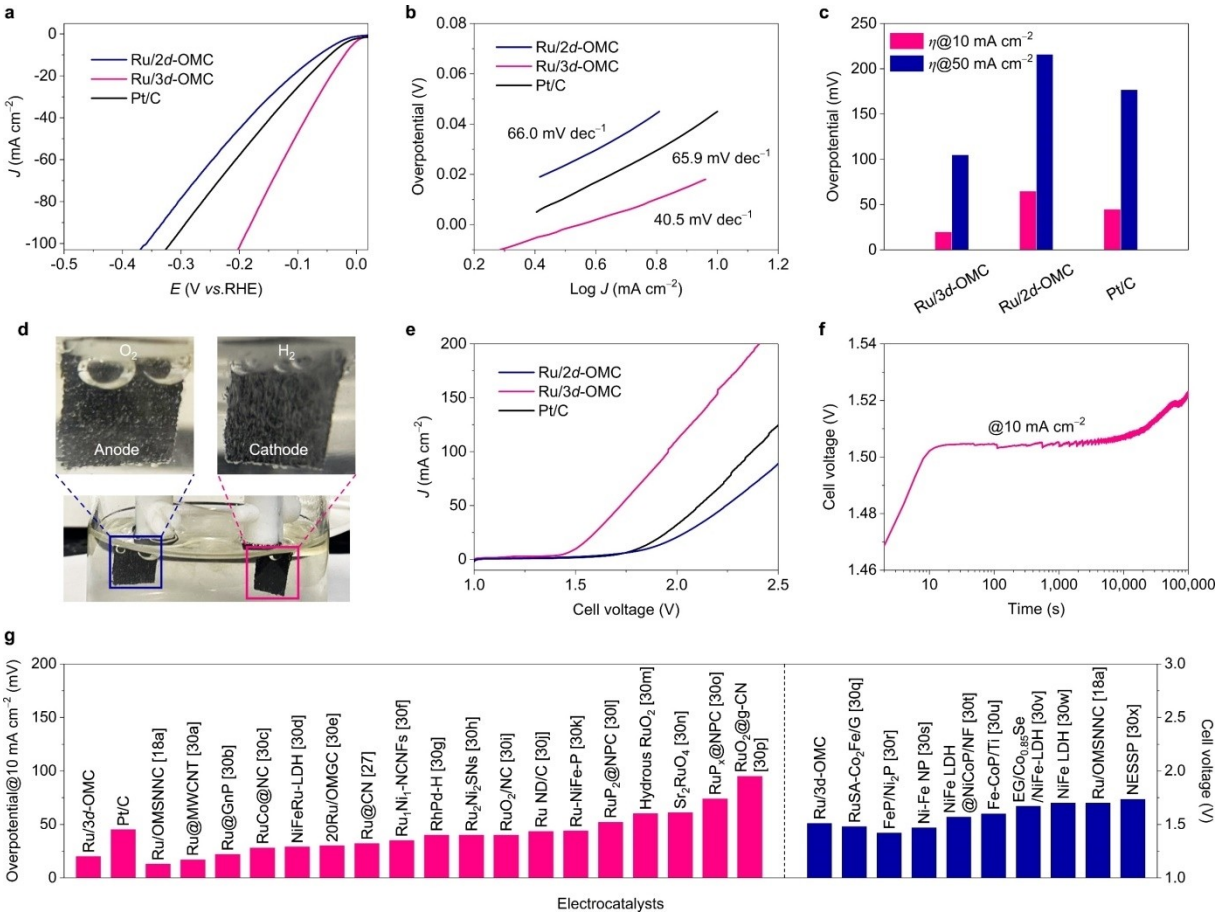

Figure 4. a) LSV curves of Ru/2*d*-OMC, Ru/3*d*-OMC, and Pt/C tested in 1 M KOH; b) Tafel plots; c) Overpotentials at 10 and 50 mA cm^{-2}; d) Photos of two-electrode device under operating condition, showing bubble formation from both electrodes during electrolysis in 1 M KOH; e) LSV curves of electrolysis cell adopting Ru/2*d*-OMC, Ru/3*d*-OMC, and Pt/C as cathodes, respectively; f) Chronopotentiometric curve at 10 mA cm^{-2} of electrolysis cell adopting Ru/3*d*-OMC; g) Comparison of the overpotentials at 10 mA cm^{-2} with recently reported HER electrocatalysts and the cell voltages at 10 mA cm^{-2} with recently reported electrolyzers in 1 M KOH.

density of 10 mA cm^{-2}, which was relatively lower than that of Pt/C (46 mV) and Ru/2*d*-OMC (80 mV), suggesting that the Ru/3*d*-OMC could also display high activity in acidic medium.

To explore the practical applications of the synthesized catalysts, we loaded the Ru/3*d*-OMC on carbon fiber paper (CFP) as the cathode to construct a two-electrode water electrolysis cell in 1 M KOH solutions and acquired their activities by LSVs as shown in Figures 4d and e. Remarkably, the cell with the Ru/3*d*-OMC cathode required only 1.51 V to reach a current density of 10 mA cm^{-2} in 1 M KOH, displaying much higher activity than those of water electrolysis cells adopting Ru/2*d*-OMC and Pt/C as cathodes. Furthermore, the voltage of water electrolysis cell adopting Ru/3*d*-OMC as cathode could be maintained at 1.51 V at 10 mA cm^{-2} for 100000 s without obvious voltage increased (Figure 4f). The excellent activity and stability of overall water splitting make Ru/3*d*-OMC become a promising candidate catalyst for practical water electrolysis applications. The overpotential and overall water splitting cell voltage of Ru/3*d*- OMC at 10 mA cm^{-2} in alkaline media were also competitive compared with other electrocatalyst reported in recent studies (Figure 4g).[18b,27,30]

To further confirm the advantages of 3*d* interconnected mesopore structures on fast diffusion of H_2, finite element method (FEM) simulations were performed on Ru/2*d*-OMC and Ru/3*d*-OMC models under a constant flux of H_2 from left to right.[31] The models of Ru/2*d*-OMC and Ru/3*d*-OMC were simplified into 2*d* plane figures due to computational cost. As the time changed from 0.1 μs to 10 μs, the fluxes of H_2 in the parallel and interconnected mesopore channels gradually increased (Figures S20 and S21). When times came to 50 μs, the fluxed of H_2 in the mesopore channels of Ru/2*d*-OMC and Ru/3*d*-OMC could maintain at a constant state (Figures 5a and b). The fluxes of H_2 also gradually decreased from left to right in both Ru/2*d*-OMC and Ru/3*d*-OMC, and the fluxes at exits were much less than those at entrance, indicating the flow of H_2 was hindered to some extent in mesopore channels. Furthermore, the concentrations (expressed by c) of H_2 in mesopore channels continued to increase along with time (Figure 5c). After 0.8 μs, the concentrations of H_2 at different areas of the mesopore channel tended to be the same (Figures S22–S24), and the

© 2022 Wiley-VCH GmbH

15213773, 2023, 3, Downloaded from https://onlinelibrary.wiley.com/doi/10.1002/anie.202212653 by University Of Adelaide, Wiley Online Library on [29/06/2024]. See the Terms and Conditions (https://onlinelibrary.wiley.com/terms-and-conditions) on Wiley Online Library for rules of use; OA articles are governed by the applicable Creative Commons License

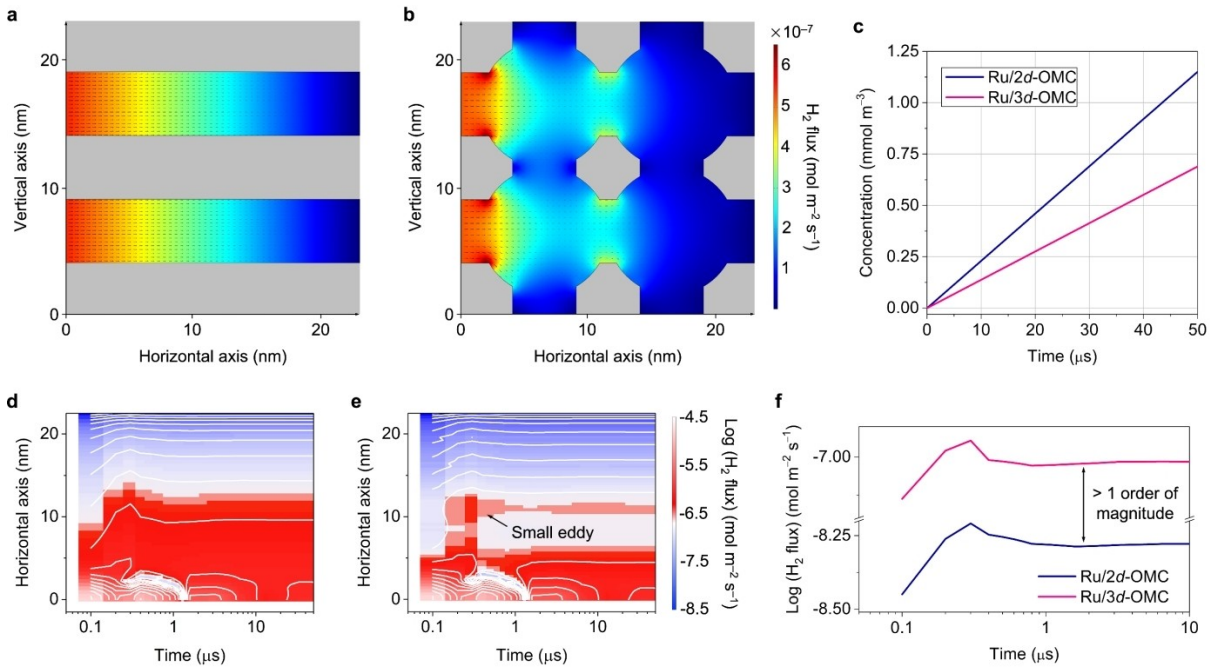

Figure 5. a), b) Flux distribution of H_2 in mesopore channels of Ru/2*d*-OMC (a) and Ru/3*d*-OMC models (b) under constant H_2 flux of 3×10^{-5} $cm^2 s^{-1}$ from left to right at the time of 50 μs; c) H_2 concentration–time curves; d), e) 2D contour plots of log(H_2 flux) as a function of time and *x*-axis position for Ru/2*d*-OMC (d) and Ru/3*d*-OMC models (e) with a fixed *y*-axis position of 16.3 nm; f) Total flux of H_2 as a function of time.

concentration of H_2 in Ru/2*d*-OMC was consistently higher than that of Ru/3*d*-OMC, indicating that more H_2 molecules were blocked in the non-interconnected parallel mesopore channels of Ru/2*d*-OMC.

From the 2*d* contour plots in Figures 5d and e, it could be observed that the fluxes of H_2 in Ru/2*d*-OMC and Ru/3*d*-OMC exhibited wild fluctuation at the entrance location of the mesopore channel within 1 μs, due to the impacts between H_2 flow and pore wall. As the horizontal axis changed from 3 nm to 23 nm, the flux in Ru/3*d*-OMC displayed a faster decrease and there was a small eddy at ≈10 nm, which could be attributed to the shunting effect of crossed channels. The log (H_2 flux)–horizontal axis curves in Figure S25 showed that the flux in Ru/3*d*-OMC was lower than that of Ru/2*d*-OMC in the range of 5 nm to 10 nm and 13 nm to 18 nm, thus indicating the interconnected mesopore structure could effectively share the flux. The 2*d* contour plots of log (H_2 flux) as a function of time and vertical axis in the Ru/3*d*-OMC also manifested that a large amount of H_2 was released through longitudinal interconnected mesopore channels (Figure S26). To further compare the mass-transport rates of H_2 in these two types of mesopore structures, we counted the total flux at the exits of Ru/3*d*-OMC and Ru/2*d*-OMC. As shown in Figure 5f, total flux at the exits of Ru/3*d*-OMC was almost ten times larger than that of Ru/2*d*-OMC, indicating that Ru/3*d*-OMC could deliver more H_2 at the same time. As for 2*d* model of Ru/3*d*-OMC, there are only four interconnected mesopores in a structure cell. However, there are eight interconnected mesopores in a structure cell of Ru/3*d*-OMC with 3*d* cubic mesopore structure in actual situation. From our FEM results, Ru/3*d*-OMC is expected to possess much higher transport efficiency in reality, indicating the significant advantages of 3*d* interconnected mesopores. If well-designed micropores with suitable sizes are introduced to connect the mesopore channels, it can be expected that transport efficiency for H_2 can be further improved.

Conclusion

In conclusion, we have developed two types of HER electrocatalysts with few-nanometer Ru nanoparticles homogeneously anchored on *p6m* and *Im*$\bar{3}$*m* ordered mesoporous carbon supports, respectively. This work provides a novel platform for understanding the pore-structural effects on diffusion efficiency of H_2 at the few-nanometer level. In Ru/2*d*-OMC, parallel mesopore channels make H_2 gas bubbles can only diffuse out in the axial direction, while criss-crossing mesopores with grade separation in Ru/3*d*-OMC allow bubbles to move freely along these interconnected channels, with fewer interruptions, thus achieving exceeding structure-enhanced HER catalytic activity of Ru/2*d*-OMC, which is even comparable to most other state-of-the-art HER catalysts. FEM results also confirm that 3*d* mesopore structure offers more diffusion paths for H_2 along the interconnected channels, and possesses much higher mass transfer rate than that of 2*d* mesopore structures. We hope this work will support a new opportunity for further optimization of electrocatalysts from the point of tuning few-nanometer mass transport through nanoscale grade seperation.

© 2022 Wiley-VCH GmbH

15213773, 2023, 3, Downloaded from https://onlinelibrary.wiley.com/doi/10.1002/anie.202212653 by University Of Adelaide, Wiley Online Library on [29/06/2024]. See the Terms and Conditions (https://onlinelibrary.wiley.com/terms-and-conditions) on Wiley Online Library for rules of use; OA articles are governed by the applicable Creative Commons License

Acknowledgements

This work was supported by the National Natural Science Foundation of China (21871159 and 22171157 to D.W., 22209073 to Z.L.), the Natural Science Foundation of Jiangsu Province (Grant No. BK20220912 to Z.L.), the Beijing Natural Science Foundation (2214061 to Z.Z.), the Science and Technology Key Project of Guangdong Province of China (2020B010188002 to D.W.), the Fundamental Research Funds for the Central Universities (WUT: 2019III012GX and 2020III002GX to J.S.W.), and the China Postdoctoral Science Foundation (2022M711607 to Z.L.). The S/TEM work was performed at the Nanostructure Research Center (NRC), which is supported by the State Key Laboratory of Advanced Technology for Materials Synthesis and Processing, and the State Key Laboratory of Silicate Materials for Architectures (all of the laboratories are at Wuhan University of Technology). We thank the 1W1B and 4B9B beamlines of Beijing Synchrotron Radiation Facility (BSRF) and the BL11B beamline of Shanghai Synchrotron Radiation Facility (SSRF) for providing beam time to support this project. Z.Z. acknowledges support from the Shuimu Tsinghua Scholar Program.

Conflict of Interest

The authors declare no conflict of interest.

Data Availability Statement

The data that support the findings of this study are available from the corresponding author upon reasonable request.

Keywords: Hydrogen Evolution Reaction · Mass Transport · Nanocatalysis · Ordered Mesoporous Structure · Single-Atom Catalysis

[1] a) E. Fabbri, M. Nachtegaal, T. Binninger, X. Cheng, B. J. Kim, J. Durst, F. Bozza, T. Graule, R. Schäublin, L. Wiles, *Nat. Mater.* **2017**, *16*, 925–931; b) H. Dotan, A. Landman, S. W. Sheehan, K. D. Malviya, G. E. Shter, D. A. Grave, Z. Arzi, N. Yehudai, M. Halabi, N. Gal, *Nat. Energy* **2019**, *4*, 786–795; c) Z. Zhuang, Y. Li, J. Huang, Z. Li, K. Zhao, Y. Zhao, L. Xu, L. Zhou, L. V. Moskaleva, L. Mai, *Sci. Bull.* **2019**, *64*, 617–624; d) P. Zhu, X. Xiong, D. Wang, *Nano Res.* **2022**, *15*, 5792–5815.

[2] a) M. Cabán-Acevedo, M. L. Stone, J. Schmidt, J. G. Thomas, Q. Ding, H. C. Chang, M. L. Tsai, J. H. He, S. Jin, *Nat. Mater.* **2015**, *14*, 1245–1251; b) J. Mahmood, F. Li, S.-M. Jung, M. S. Okyay, I. Ahmad, S. J. Kim, N. Park, H. Y. Jeong, J. B. Baek, *Nat. Nanotechnol.* **2017**, *12*, 441–446; c) D. Voiry, H. Yamaguchi, J. Li, R. Silva, D. C. Alves, T. Fujita, M. Chen, T. Asefa, V. B. Shenoy, G. Eda, *Nat. Mater.* **2013**, *12*, 850–855; d) Z. Zhuang, J. Huang, Y. Li, L. Zhou, L. Mai, *ChemElectroChem* **2019**, *6*, 3570–3589.

[3] a) G. B. Darband, M. Aliofkhazraei, S. Shanmugam, *Renewable Sustainable Energy Rev.* **2019**, *114*, 109300; b) A. Angulo, P. van der Linde, H. Gardeniers, M. Modestino, D. F. Rivas, *Joule* **2020**, *4*, 555–579; c) A. R. Zeradjanin, P. Narangoda, I. Spanos, J. Masa, R. Schlögl, *Curr. Opin. Electrochem.* **2021**, *30*, 100797.

[4] a) H. Zhou, F. Yu, Q. Zhu, J. Sun, F. Qin, L. Yu, J. Bao, Y. Yu, S. Chen, Z. Ren, *Energy Environ. Sci.* **2018**, *11*, 2858–2864; b) Y. Xu, C. Wang, Y. Huang, J. Fu, *Nano Energy* **2021**, *80*, 105545.

[5] a) T. Kou, S. Wang, R. Shi, T. Zhang, S. Chiovoloni, J. Q. Lu, W. Chen, M. A. Worsley, B. C. Wood, S. E. Baker, *Adv. Energy Mater.* **2020**, *10*, 2002955; b) Y. J. Kim, A. Lim, J. M. Kim, D. Lim, K. H. Chae, E. N. Cho, H. J. Han, K. U. Jeon, M. Kim, G. H. Lee, *Nat. Commun.* **2020**, *11*, 4921; c) F. Yang, M. J. Kim, M. Brown, B. J. Wiley, *Adv. Energy Mater.* **2020**, *10*, 2001174; d) B. You, Y. Sun, *Acc. Chem. Res.* **2018**, *51*, 1571–1580; e) J. Kibsgaard, I. Chorkendorff, *Nat. Energy* **2019**, *4*, 430–433; f) Z. W. Seh, J. Kibsgaard, C. F. Dickens, I. Chorkendorff, J. K. Nørskov, T. F. Jaramillo, *Science* **2017**, *355*, eaad4998.

[6] a) S. Shen, Z. Lin, K. Song, Z. Wang, L. Huang, L. Yan, F. Meng, Q. Zhang, L. Gu, W. Zhong, *Angew. Chem. Int. Ed.* **2021**, *60*, 12360–12365; *Angew. Chem.* **2021**, *133*, 12468–12473; b) J. Kibsgaard, T. F. Jaramillo, F. Besenbacher, *Nat. Chem.* **2014**, *6*, 248–253; c) J. Huang, Z. Zhuang, Y. Zhao, J. Chen, Z. Zhuo, Y. Liu, N. Lu, H. Li, T. Zhai, *Angew. Chem. Int. Ed.* **2022**, *61*, e202203522; *Angew. Chem.* **2022**, *134*, e202203522.

[7] a) D. Yan, Y. Li, J. Huo, R. Chen, L. Dai, S. Wang, *Adv. Mater.* **2017**, *29*, 1606459; b) Y. Zhang, L. Tao, C. Xie, D. Wang, Y. Zou, R. Chen, Y. Wang, C. Jia, S. Wang, *Adv. Mater.* **2020**, *32*, 1905923.

[8] a) Y. Chen, Z. Lai, X. Zhang, Z. Fan, Q. He, C. Tan, H. Zhang, *Nat. Chem. Rev.* **2020**, *4*, 243–256; b) Q. Lu, A.-L. Wang, Y. Gong, W. Hao, H. Cheng, J. Chen, B. Li, N. Yang, W. Niu, J. Wang, *Nat. Chem.* **2018**, *10*, 456–461.

[9] a) H. Mistry, A. S. Varela, S. Kühl, P. Strasser, B. R. Cuenya, *Nat. Rev. Mater.* **2016**, *1*, 16009; b) Y. Li, Y. Sun, Y. Qin, W. Zhang, L. Wang, M. Luo, H. Yang, S. Guo, *Adv. Energy Mater.* **2020**, *10*, 1903120.

[10] a) J. Hao, Z. Zhuang, K. Cao, G. Gao, C. Wang, F. Lai, S. Lu, P. Ma, W. Dong, T. Liu, *Nat. Commun.* **2022**, *13*, 2662; b) D. Deng, K. Novoselov, Q. Fu, N. Zheng, Z. Tian, X. Bao, *Nat. Nanotechnol.* **2016**, *11*, 218–230.

[11] a) W. Yang, S. Chen, *Chem. Eng. J.* **2020**, *393*, 124726; b) J. Linnemann, K. Kanokkanchana, K. Tschulik, *ACS Catal.* **2021**, *11*, 5318–5346.

[12] a) F. Song, W. Li, J. Yang, G. Han, P. Liao, Y. Sun, *Nat. Commun.* **2018**, *9*, 4531; b) I. Roger, M. A. Shipman, M. D. Symes, *Nat. Chem. Rev.* **2017**, *1*, 0003.

[13] a) R. Liu, Z. Gong, J. Liu, J. Dong, J. Liao, H. Liu, H. Huang, J. Liu, M. Yan, K. Huang, *Adv. Mater.* **2021**, *33*, 2103533.

[14] L. Wan, Z. Xu, Q. Xu, P. Wang, B. Wang, *Energy Environ. Sci.* **2022**, *15*, 1882–1892.

[15] a) C. Rakousky, U. Reimer, K. Wippermann, M. Carmo, W. Lueke, D. Stolten, *J. Power Sources* **2016**, *326*, 120–128; b) N. U. Hassan, M. Mandal, B. Zulevi, P. A. Kohl, W. E. Mustain, *Electrochim. Acta* **2022**, *409*, 140001.

[16] a) D. Kong, H. Wang, Z. Lu, Y. Cui, *J. Am. Chem. Soc.* **2014**, *136*, 4897–4900; b) K. Wang, D. Xi, C. Zhou, Z. Shi, H. Xia, G. Liu, G. Qiao, *J. Mater. Chem. A* **2015**, *3*, 9415–9420.

[17] a) N. Han, K. R. Yang, Z. Lu, Y. Li, W. Xu, T. Gao, Z. Cai, Y. Zhang, V. S. Batista, W. Liu, *Nat. Commun.* **2018**, *9*, 924; b) S. Wang, S. Lai, P. Li, T. Gao, K. Sun, X. Ding, T. Xie, C. Wu, X. Li, Y. Kuang, *J. Power Sources* **2019**, *436*, 226867.

[18] a) T. Schuler, J. M. Ciccone, B. Krentscher, F. Marone, C. Peter, T. J. Schmidt, F. N. Büchi, *Adv. Energy Mater.* **2020**, *10*, 1903216; b) Y. L. Wu, X. Li, Y. S. Wei, Z. Fu, W. Wei, X. T. Wu, Q. L. Zhu, Q. Xu, *Adv. Mater.* **2021**, *33*, 2006965; c) Q. Xu, Y. Liu, H. Jiang, Y. Hu, H. Liu, C. Li, *Adv. Energy Mater.* **2019**, *9*, 1802553; d) A. I. Douka, Y. Xu, H. Yang, S. Zaman,

© 2022 Wiley-VCH GmbH

15213773, 2023, 3, Downloaded from https://onlinelibrary.wiley.com/doi/10.1002/anie.202212653 by University Of Adelaide, Wiley Online Library on [29/06/2024]. See the Terms and Conditions (https://onlinelibrary.wiley.com/terms-and-conditions) on Wiley Online Library for rules of use; OA articles are governed by the applicable Creative Commons License

Y. Yan, H. Liu, M. A. Salam, B. Y. Xia, *Adv. Mater.* **2020**, *32*, 2002170.

[19] a) J. Shen, G. Liu, Y. Han, W. Jin, *Nat. Rev. Mater.* **2021**, *6*, 294–312; b) Z. Liu, Y. Du, P. Zhang, Z. Zhuang, D. Wang, *Matter* **2021**, *4*, 3161–3194.

[20] a) S. Ye, F. Luo, T. Xu, P. Zhang, H. Shi, S. Qin, J. Wu, C. He, X. Ouyang, Q. Zhang, *Nano Energy* **2020**, *68*, 104301; b) Q. Hu, K. Gao, X. Wang, H. Zheng, J. Cao, L. Mi, Q. Huo, H. Yang, J. Liu, C. He, *Nat. Commun.* **2022**, *13*, 3958; c) A. Wang, J. Li, T. Zhang, *Nat. Chem. Rev.* **2018**, *2*, 65–81; d) Z. Zhuang, Y. Li, Y. Li, J. Huang, B. Wei, R. Sun, Y. Ren, J. Ding, J. Zhu, Z. Lang, L. V. Moskaleva, C. He, Y. Wang, Z. Wang, D. Wang, Y. Li, *Energy Environ. Sci.* **2021**, *14*, 1016.

[21] a) Z. Zhuang, Y. Li, R. Yu, L. Xia, J. Yang, Z. Lang, J. Zhu, J. Huang, J. Wang, Y. Wang, *Nat. Catal.* **2022**, *5*, 300–310; b) R. Li, D. Wang, *Nano Res.* **2022**, *15*, 6888–6923; c) X. Zheng, B. Li, Q. Wang, D. Wang, Y. Li, *Nano Res.* **2022**, *15*, 7806–7839; d) Z. Zhuang, L. Xia, J. Huang, P. Zhu, Y. Li, C. Ye, M. Xia, R. Yu, Z. Lang, J. Zhu, L. Zheng, Y. Wang, T. Zhai, Y. Zhao, S. Wei, J. Li, D. Wang, Y. Li, *Angew. Chem. Int. Ed.* **2022**, *61*, e202212335; *Angew. Chem.* **2022**, *134*, e202212335.

[22] a) H. Zhang, W. Zhou, X. F. Lu, T. Chen, X. W. Lou, *Adv. Energy Mater.* **2020**, *10*, 2000882; b) X. K. Wan, H. B. Wu, B. Y. Guan, D. Luan, X. W. Lou, *Adv. Mater.* **2020**, *32*, 1901349; c) X. Xiao, X. Wang, X. Jiang, S. Song, D. Huang, L. Yu, Y. Zhang, S. Chen, M. Wang, Y. Shen, *Small Methods* **2020**, *4*, 1900796; d) J. Yang, W. Li, K. Xu, S. Tan, D. Wang, Y. Li, *Angew. Chem. Int. Ed.* **2022**, *61*, e202200366; *Angew. Chem.* **2022**, *134*, e202200366; e) W. Li, R. Yang, D. Wang, *Angew. Chem. Int. Ed.* **2022**, *61*, e202213318; *Angew. Chem.* **2022**, *134*, e202213318.

[23] a) J. Wordsworth, T. M. Benedetti, S. V. Somerville, W. Schuhmann, R. D. Tilley, J. J. Gooding, *Angew. Chem. Int. Ed.* **2022**, *61*, e202200755; *Angew. Chem.* **2022**, *134*, e202200755; b) X. Li, L. Liu, X. Ren, J. Gao, Y. Huang, B. Liu, *Sci. Adv.* **2020**, *6*, eabb6833.

[24] a) G. H. Wang, Z. Cao, D. Gu, N. Pfänder, A. C. Swertz, B. Spliethoff, H. J. Bongard, C. Weidenthaler, W. Schmidt, R. Rinaldi, *Angew. Chem. Int. Ed.* **2016**, *55*, 8850–8855; *Angew. Chem.* **2016**, *128*, 8996–9001; b) J. Wei, D. Zhou, Z. Sun, Y. Deng, Y. Xia, D. Zhao, *Adv. Funct. Mater.* **2013**, *23*, 2322–2328; c) D. Liu, J. H. Lei, L.-P. Guo, D. Qu, Y. Li, B. L. Su, *Carbon* **2012**, *50*, 476–487.

[25] a) J. Miao, P. Ercius, S. J. Billinge, *Science* **2016**, *353*, aaf2157; b) H. Song, Y. Yang, J. Geng, Z. Gu, J. Zou, C. Yu, *Adv. Mater.* **2019**, *31*, 1801564.

[26] B. Lu, L. Guo, F. Wu, Y. Peng, J. E. Lu, T. J. Smart, N. Wang, Y. Z. Finfrock, D. Morris, P. Zhang, *Nat. Commun.* **2019**, *10*, 631.

[27] J. Wang, Z. Wei, S. Mao, H. Li, Y. Wang, *Energy Environ. Sci.* **2018**, *11*, 800–806.

[28] a) Z. Jiang, W. Sun, H. Shang, W. Chen, T. Sun, H. Li, J. Dong, J. Zhou, Z. Li, Y. Wang, *Energy Environ. Sci.* **2019**, *12*, 3508–3514; b) J. Wan, Z. Zhao, H. Shang, B. Peng, W. Chen, J. Pei, L. Zheng, J. Dong, R. Cao, R. Sarangi, *J. Am. Chem. Soc.* **2020**, *142*, 18, 8431–8439; c) R. Arrigo, M. E. Schuster, Z. Xie, Y. Yi, G. Wowsnick, L. L. Sun, K. E. Hermann, M. Friedrich, P. Kast, M. Hävecker, A. Knop-Gericke, R. Schlögl, *ACS Catal.* **2015**, *5*, 2740–2753.

[29] W. Gao, Y. Wan, Y. Dou, D. Zhao, *Adv. Energy Mater.* **2011**, *1*, 115–123.

[30] a) D. H. Kweon, M. S. Okyay, S. J. Kim, J. P. Jeon, H. J. Noh, N. Park, J. Mahmood, J. B. Baek, *Nat. Commun.* **2020**, *11*, 1278; b) F. Li, G. Han, H. Noh, I. Ahmad, I. Jeon, J. Baek, *Adv. Mater.* **2018**, *30*, 1803676; c) J. Su, Y. Yang, G. Xia, J. Chen, P. Jiang, Q. Chen, *Nat. Commun.* **2017**, *8*, 14969; d) G. Chen, T. Wang, J. Zhang, P. Liu, H. Sun, X. Zhuang, M. Chen, X. Feng, *Adv. Mater.* **2018**, *30*, 1706279; e) D. S. Baek, K. A. Lee, J. Park, J. H. Kim, J. Lee, J. S. Lim, S. Y. Lee, T. J. Shin, H. Y. Jeong, J. S. Son, S. J. Kang, J. Y. Kim, S. H. Joo, *Angew. Chem. Int. Ed.* **2021**, *60*, 1441; *Angew. Chem.* **2021**, *133*, 1461; f) M. Li, H. Wang, W. Zhu, W. Li, C. Wang, X. Lu, *Adv. Sci.* **2020**, *7*, 1901833; g) J. Fan, J. Wu, X. Cui, L. Gu, Q. Zhang, F. Meng, B.-H. Lei, D. J. Singh, W. Zheng, *J. Am. Chem. Soc.* **2020**, *142*, 3645; h) J. Ding, Q. Shao, Y. Feng, X. Huang, *Nano Energy* **2018**, *47*, 1; i) C. Z. Yuan, Y. F. Jiang, Z. W. Zhao, S. J. Zhao, X. Zhou, T. Y. Cheang, A. W. Xu, *ACS Sustainable Chem. Eng.* **2018**, *6*, 11529; j) K. Gao, Y. Wang, Z. Wang, Z. Zhu, J. Wang, Z. Luo, C. Zhang, X. Huang, H. Zhang, W. Huang, *Chem. Commun.* **2018**, *54*, 4613–4616; k) M. Qu, Y. Jiang, M. Yang, S. Liu, Q. Guo, W. Shen, M. Li, R. He, *Appl. Catal. B* **2020**, *263*, 118324; l) Z. Pu, I. S. Amiinu, Z. Kou, W. Li, S. Mu, *Angew. Chem. Int. Ed.* **2017**, *56*, 11559; *Angew. Chem.* **2017**, *129*, 11717; m) J. Lee, S. A. S. Shah, P. J. Yoo, B. Lim, *Chem. Phys. Lett.* **2017**, *673*, 89; n) Y. Zhu, H. A. Tahini, Z. Hu, J. Dai, Y. Chen, H. Sun, W. Zhou, M. Liu, S. C. Smith, H. Wang, Z. Shao, *Nat. Commun.* **2019**, *10*, 14; o) Q. Chi, W. K. Gao, J. H. Lin, B. Dong, K. L. Yan, J. F. Qin, B. Liu, Y. M. Chai, C. G. Liu, *ChemSusChem* **2018**, *11*, 743–752; p) T. Bhowmik, M. K. Kundu, S. Barman, *ACS Appl. Mater. Interfaces* **2016**, *8*, 28678; q) J. Lee, A. Kumar, T. Yang, X. Liu, A. R. Jadhav, G. H. Park, Y. Hwang, J. Yu, C. T. K. Nguyen, Y. Liu, S. Ajmal, M. G. Kim, H. Lee, *Energy Environ. Sci.* **2020**, *13*, 5152; r) F. Yu, H. Zhou, Y. Huang, J. Sun, F. Qin, J. Bao, W. A. Goddard III, S. Chen, Z. Ren, *Nat. Commun.* **2018**, *9*, 2551; s) B. H. R. Suryanto, Y. Wang, R. K. Hocking, W. Adamson, C. Zhao, *Nat. Commun.* **2019**, *10*, 5599; t) H. Zhang, X. Li, A. Hähnel, V. Naumann, C. Lin, S. Azimi, S. L. Schweizer, A. W. Maijenburg, R. B. Wehrspohn, *Adv. Funct. Mater.* **2018**, *28*, 1706847; u) C. Tang, R. Zhang, W. Lu, L. He, X. Jiang, A. M. Asiri, X. Sun, *Adv. Mater.* **2017**, *29*, 1602441; v) Y. Hou, M. R. Lohe, J. Zhang, S. Liu, X. Zhuang, X. Feng, *Energy Environ. Sci.* **2016**, *9*, 478; w) J. Luo, J.-H. Im, M. T. Mayer, M. Schreier, M. K. Nazeeruddin, N. G. Park, S. D. Tilley, H. Fan, M. Grätzel, *Science* **2014**, *345*, 1593; x) M. S. Balogun, W. Qiu, Y. Huang, H. Yang, R. Xu, W. Zhao, G. R. Li, H. Ji, Y. Tong, *Adv. Mater.* **2017**, *29*, 1702095.

[31] T. Sen, M. Barisik, *Colloid Polym. Sci.* **2019**, *297*, 1365–1373.

Manuscript received: August 27, 2022
Accepted manuscript online: November 18, 2022
Version of record online: December 12, 2022

© 2022 Wiley-VCH GmbH

15213773, 2023, 3, Downloaded from https://onlinelibrary.wiley.com/doi/10.1002/anie.202212653 by University Of Adelaide, Wiley Online Library on [29/06/2024]. See the Terms and Conditions (https://onlinelibrary.wiley.com/terms-and-conditions) on Wiley Online Library for rules of use; OA articles are governed by the applicable Creative Commons License